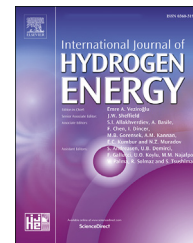


Available online at www.sciencedirect.com

ScienceDirect

journal homepage: www.elsevier.com/locate/he

Thermochemical method for controlling pore structure to enhance hydrogen storage capacity of biochar



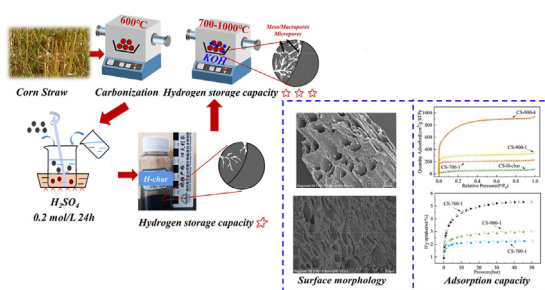
Lihua Deng, Yijun Zhao*, Shaozeng Sun, Dongdong Feng, Wenda Zhang

School of Energy Science and Engineering, Harbin Institute of Technology, PR China

HIGHLIGHTS

- The BET area and microporosity of biochar can reach 2801.88 m²/g and 96.56%.
- The factors affecting the conversion of carbon nanopores were clarified.
- Hydrogen uptake of biochar at −196 °C was 2.53 wt% at 1 bar and 5.32 wt% at 50 bar.
- The relationship between pore structure and hydrogen storage capacity was discussed.
- The hydrogen adsorption of the graded pores under different pressures was analyzed.

GRAPHICAL ABSTRACT



ARTICLE INFO

Article history:

Received 1 January 2023

Received in revised form

15 February 2023

Accepted 7 March 2023

Available online 22 March 2023

Keywords:

Biochar

Activation

Pore structure

ABSTRACT

Developing new carbon-based hydrogen storage materials can significantly promote solid-state hydrogen storage technology. Biochar with high hydrogen storage capacity can be prepared by KOH melt activation, which has a high proportion of micropores (96.56%) compared with the porous carbon in the existing literature. Its specific surface area and pore volume are 2801.88 m²/g and 1.44 cm³/g, respectively. The size of the nanopores is affected by the activation ratio, but the temperature has little effect at the low activation ratio. SEM results show that the KOH activation process gradually shifts from the biochar's inside to the outside. A low KOH/char ratio (less than 2:1) can promote the formation of small aromatic rings. Due to its high specific surface area and microporosity, the absolute adsorption capacity of hydrogen in biochar is 2.53 wt% at −196 °C and 1 bar, rising to 5.32 wt% at 50 bar. The hydrogen adsorption process conforms to the Langmuir model.

* Corresponding author.

E-mail addresses: 15504663573@163.com (L. Deng), zhaoyijun@hit.edu.cn (Y. Zhao), sunsz@hit.edu.cn (S. Sun), 08031175@163.com (D. Feng), zhangwenda1992@yeah.net (W. Zhang).

<https://doi.org/10.1016/j.ijhydene.2023.03.084>

0360-3199/© 2023 Hydrogen Energy Publications LLC. Published by Elsevier Ltd. All rights reserved.

Hydrogen storage
Isothermal adsorption model

Microporous, mesoporous, and macroporous exhibit different hydrogen adsorption characteristics in various pressure ranges. However, ultramicroporous (<0.7 nm) always plays a decisive role in the hydrogen storage of biochar.

© 2023 Hydrogen Energy Publications LLC. Published by Elsevier Ltd. All rights reserved.

Introduction

As a zero-carbon and sustainable clean energy, hydrogen energy occupies a vital position in the energy architecture to achieve carbon neutrality. However, the hydrogen storage issues seriously restrict the further development of the hydrogen energy industry. Traditional high-pressure compression and ultra-low temperature liquid storage methods face two core bottlenecks: high cost, low efficiency and poor safety [1]. Using solid materials for hydrogen adsorption is considered a safer and more economical method [2,3]. At present, solid hydrogen storage materials are mainly divided into metal hydrides, composite hydrides, metal-organic frameworks (MOFs), and carbon-based nanomaterials. The theoretical hydrogen storage capacity of the first three materials is high, but the disadvantages of low hydrogen storage capacity per unit weight, high hydrogen desorption temperature and slow desorption kinetics, easy inactivation, and high regeneration cost limit their large-scale preparation in the future. Carbon-based materials have the advantages of low density, large surface area, high chemical stability, and fast adsorption/desorption kinetics [4–7], which are the critical research objects of solid hydrogen storage materials.

Renewable and low-cost biomass not only enables the preparation of activated carbon with high adsorption performance, but also has proven to have high potential for hydrogen storage [8–11]. For example, Kızılduman et al. [3] synthesized porous carbon spheres by hydrothermal carbonization of rice husks, and the hydrogen storage capacity was determined to be 1.1 wt% at $-196\text{ }^{\circ}\text{C}$ and 30 bar. Rowlandson et al. [8] found that activated carbon from lignin had a high surface area ($>1000\text{ m}^2/\text{g}$) and a hydrogen storage capacity of 1.8 wt% at $-196\text{ }^{\circ}\text{C}$ and 1 bar. And Wang et al. [12] prepared fungus-based porous carbon, achieving excellent hydrogen absorption of up to 2.4 wt% at $-196\text{ }^{\circ}\text{C}$ and 1 bar.

Most studies have found that the hydrogen storage capacity of carbon-based materials is linearly related to their specific surface area [9,13–15]. Chahine et al. [16,17] showed that the maximum hydrogen storage capacity of carbon-based materials at $-196\text{ }^{\circ}\text{C}$ is related to its specific surface area, and the hydrogen storage capacity per $500\text{ m}^2/\text{g}$ BET surface area is 1 wt%. Zhang et al. [18] used biomass pyrolysis steam as the carbon source and prepare a porous carbon with a maximum specific surface area of $1703\text{ m}^2/\text{g}$. The hydrogen adsorption capacity of the carbon material could reach $170.12\text{ cm}^3/\text{g}$ (1.53 wt%) at $-196\text{ }^{\circ}\text{C}$ and 1 bar. The above results show that the hydrogen storage using biochar material does not strictly follow Chahine's rule, and its adaptability needs to be further discussed.

The optimal pore size for the adsorption of carbon-based materials varies with the adsorption medium. Cabria et al.

[19] found that the optimal pore size for hydrogen adsorption in activated carbon at room temperature was about 0.6 nm, and theoretical studies showed that 0.5–0.7 nm or two or three times the diameter of hydrogen molecules was the optimal size for hydrogen storage [20–22]. In addition, the increase in the average micropore size can effectively reduce the adsorption potential of hydrogen. A pore size greater than 0.7 nm can also effectively improve the hydrogen storage capacity under low-temperature conditions [23]. Therefore, it is necessary to accurately construct sub-nanometer pores and increase the proportion to achieve high hydrogen storage capacity of carbon-based materials. Romanos et al. [24] experimentally demonstrated that the amount of sub-nanometer (<1 nm) and nanoporosity (1–5 nm) of char could be controlled by selecting the appropriate activation temperature and KOH/char ratio. Nam et al. [25] used the KOH activation method to prepare rice husk-based carbon materials with high adsorption performance. Huang et al. [26] successfully prepared activated carbon materials with a maximum specific surface area of $3400\text{ m}^2/\text{g}$ by KOH activation and found that their specific surface area increased with the increase of KOH/char ratio and had high hydrogen storage capacity at low temperature and pressure. Dogan et al. [27] used KOH activated tangerine peel to synthesize activated carbon samples, and the hydrogen storage capacity at $-196\text{ }^{\circ}\text{C}$ low temperature at 30 bar pressure is 1.11 wt%. In summary, the biochar materials with a specific hydrogen storage capacity can be prepared by KOH activation. Whereas the relationship between the pore structure parameters and the hydrogen storage capacity of biochar needs to be further explored for an in-depth understanding of the activation process to regulate the pore structure to strengthen its hydrogen storage capacity.

In this study, the thermochemical conversion process of straw is regulated by changing the activation temperature and KOH/char ratio. And the mutual conversion of sub-nanometer and nanopores is handled, aiming to achieve high-density hydrogen storage of biochar materials. Before and after the experiment, AAEMs that may have potential impact were removed by pickling, and the relationship between the pore structure of biochar and its hydrogen storage capacity was clarified, so as to further optimize the solid hydrogen storage system and improve its commercial feasibility. Finally, the high-value utilization of biomass is realized.

Experimental and methods

Materials

The corn straw produced in the surrounding areas of Harbin in China, which was selected as raw material. The biomass was crushed and sieved to 53–125 μm , dried at $105\text{ }^{\circ}\text{C}$ for 12 h to

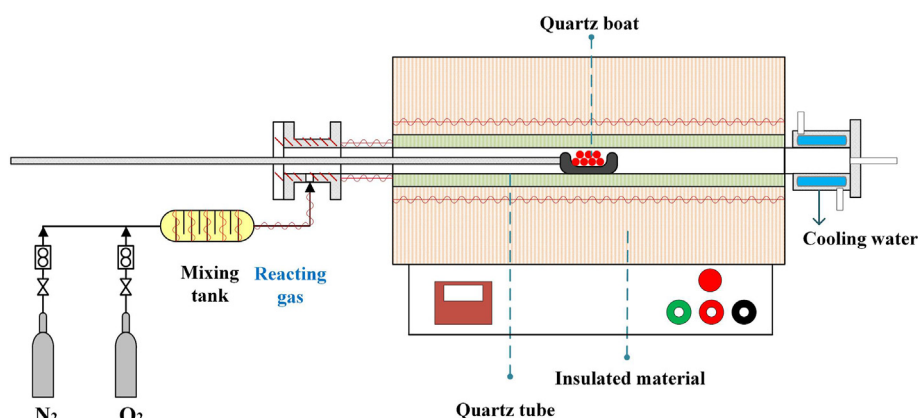
Table 1 – Proximate analysis and ultimate analysis of corn straws.

Sample	Proximate analysis (wt.%)				Ultimate analysis (wt.%)				
	M _{ad}	A _{ad}	V _{ad}	FC _{ad}	C _{ad}	H _{ad}	O _{ad,*}	N _{ad}	S _{ad}
Corn straws	9.40	1.30	71.00	18.30	43.28	5.60	50.39	0.63	0.10

Note: ad = air dry basis, * = by difference.

Table 2 – Relative content of metals and metal oxides in corn straws (wt.%).

	Na	Mg	Al	Si	P	S	K	Ca	Cr	Fe	Cu
Corn straws	0.20	0.20	0.02	0.58	0.12	0.07	2.66	0.72	0.03	0.04	0.02
	Na ₂ O	MgO	Al ₂ O ₃	SiO ₂	P ₂ O ₅	SO ₃	K ₂ O	CaO	Cr ₂ O ₃	Fe ₂ O ₃	CuO
Corn straws	0.27	0.33	0.03	1.21	0.25	0.16	2.76	0.80	0.03	0.04	0.02

**Fig. 1 – Thermal conversion experimental system of biochar.**

obtain the raw material. The ultimate analysis and proximate analysis of biomass are shown in Table 1. XRF (X-ray Fluorescence) tests were also performed on corn straws, and the relative content of metals and oxides is shown in Table 2.

Biochar preparation, pickling, and activation

The dried corn straw is pyrolyzed and carbonized in a constant-temperature tube furnace. The temperature is heated to 600 °C at a heating rate of 10 °C/min under a nitrogen atmosphere of 1 L/min. Each experiment is loaded with 4 ± 0.010 g sample using a quartz boat. As shown in Fig. 1, the quartz boat containing the sample is placed in the center area of the tube furnace, and the experiment is started after 20min of nitrogen puffing. When the temperature reaches 600 °C, hold it for 30min, and then quickly push the sample into the cooling sleeve on the right and take it out after cooling it down for 20min.

To avoid the effect of AAEMs on KOH-activated biochar, the prepared biochar was mixed with 0.2 mol/L H₂SO₄ solutions according to the liquid-solid ratio of 40:1 and stirred in an air atmosphere for 24 h at room temperature in a magnetic stirrer [28,29]. The mixture is filtered and washed repeatedly with deionized water until the PH of the wash solution is constant. After the sample is dried, the H-biochar (H-type) is obtained.

The activation conditions of KOH and H-biochar are shown in Table 3. The CO₂ activation produced by the dissolution of

Table 3 – Experimental working conditions and sample codes.

Sample	Temperature (°C)	KOH/char	Sample mass (g)
H-biochar	700	1 : 1	2
H-biochar	800	1 : 1	2
H-biochar	900	1 : 1	2
H-biochar	1000	1 : 1	2
H-biochar	900	2 : 1	2
H-biochar	900	3 : 1	2
H-biochar	900	4 : 1	2

SiO₂ in char by KOH and the decomposition of K₂CO₃, and the expansion of the carbon lattice by metal K in the carbon sheet layer promote the development of pores [24,30]. During the activation process, the active components such as K₂O, K₂CO₃, and gaseous metal K are affected by the ratio of KOH/char and the change in temperature range, thereby acting on the pore development of char [31]. Therefore, we select the ratio of KOH/char from 1:1 to 4:1 in different temperature intervals to study its effect on porosity.

The atmosphere during KOH activation is N₂, the gas flow rate is 1 L/min. The sample amount is 2 ± 0.010 g per experiment, and the samples are loaded with nickel crucibles. The quartz tube of the tube furnace was replaced with a corundum tube, the sample was mixed with a certain mass ratio of KOH and fully ground in the crucible. The nickel crucible containing

the sample was placed in the central area of the tube furnace, and the experiment was started after purging through N_2 for 20min, and the heating rate was $5^\circ C/min$. When the specified temperature is reached, it is maintained for 30min, and then cooled to below $200^\circ C$ at a cooling rate of $5^\circ C/min$. The sample is quickly pushed into the cooling sleeve on the right, and the sample is taken out after 20min cooling. To avoid the influence of the residual K-containing substances after activation on the subsequent hydrogen storage test, the collected samples were mixed with a $0.2\text{ mol/L H}_2\text{SO}_4$ solution with a liquid-solid ratio of 40:1 and stirred in an air atmosphere for 4 h in a magnetic stirrer at room temperature. The mixture is filtered and washed repeatedly with deionized water until the pH of the wash solution is constant. After the sample is dried, the final biochar material is obtained. The name of the sample is CS-A-B (A refers to temperature, B refers to activation ratio). For example, CS-900-1 represents biochar obtained after activation at $900^\circ C$ and KOH/char at 1:1.

Material characterization

Nitrogen adsorption and desorption experiments were performed using BSD-PM high-performance specific surface area analyzer (A Company named Beijing Best) at $-196^\circ C$. The sample was degassed at $250^\circ C$ for 180 min, and the specific surface area was calculated using the Brunauer-Emmett-Teller (BET) method. The pore size distribution of the carbon material was determined by the Barrett-Joyner-Halenda (BJH) method and the Horvath-Kawazoe (H-K) method [32].

Use a scanning electron microscope (SEM, Regulus 8100) to observe the apparent morphology of biochar. The accelerating voltage is $0.5\text{--}30\text{ kV}$, and the secondary electron resolution is 0.8 nm (accelerating voltage 15 kV). Some areas with typical topographic structures are characterized by a magnification of 50,000 [33].

The thermal stability of activated biochar materials was determined by a thermogravimetric analyzer (TGA/SDTA851e, Mettler-Toledo) operating at atmospheric pressure. The measurement temperature is $25^\circ C$ to $900^\circ C$ in air atmosphere (30 mL/min), the heating rate is $10^\circ C/min$, and the dosage is $6 \pm 0.050\text{ mg}$ each time.

Raman spectroscopy (inVia Reflex) is used to test the carbon skeleton structure of biochar. The laser wavelength tested was 532 nm and the scanning range was $4000\text{--}400\text{ cm}^{-1}$. Spectra in the range of $1800\text{--}1000\text{ cm}^{-1}$ were analyzed.

Hydrogen uptake measurements

Before measurement, the sample is degassed in a vacuum at $300^\circ C$ for 120 min. Hydrogen physical adsorption isotherms with temperatures of $-196^\circ C$ and pressure ranges of $1\text{--}50\text{ bar}$ are collected using a PSD-PH device. The automatic constant system on the surface of liquid nitrogen maintains a test temperature stability of $-196^\circ C$, the pressure accuracy of the device reaches 0.01% FS, and the temperature control accuracy is $\pm 0.1^\circ C$.

The calculation method of the excess adsorption capacity of hydrogen measured by the experiment and the absolute adsorption capacity converted is as follows. The excess adsorption amount m_{ex} can be calculated by Equation (1). The

adsorption phase density of hydrogen is calculated by Equation (2), and finally, the absolute adsorption capacity of hydrogen is calculated by Equation (3).

$$m_{\text{ex}} = \Delta m - m_{\text{sc}} - m_{\text{s}} + (V_{\text{sc}} + V_{\text{s}})\rho_{\text{g}} \quad (1)$$

$$V_{\text{ex}} = \frac{V_{\text{L}}P}{P_{\text{L}} + P} \times \left(1 - \frac{\rho_{\text{g}}}{\rho_{\text{a}}}\right) \quad (2)$$

$$m_{\text{abs}} = m_{\text{ex}} / \left(1 - \frac{\rho_{\text{g}}}{\rho_{\text{a}}}\right) \quad (3)$$

m_{ex} indicates the excess adsorption capacity of hydrogen, g; Δm represents the reading of the maglev balance, g; m_{sc} indicates the mass of the sample barrel, g; m_{s} suggests the mass of the sample, g; V_{sc} represents the reading of the maglev balance, g; m_{sc} indicates the mass of the sample barrel, g; m_{s} suggests the mass of the sample, g; V_{sc} represents the volume of the sample barrel, cm^3 ; V_{s} indicates the volume of the sample, cm^3 ; ρ_{g} indicates the density of hydrogen gas at different pressure points, g/cm^3 ; V_{ex} indicates the excess adsorption volume, cm^3/g ; V_{L} means Langmuir volume, cm^3/g ; P_{L} stands for Langmuir pressure, MPa; P indicates the experimental pressure, MPa; ρ_{a} : The adsorption phase density, g/cm^3 , the attached adsorption phase density value is between the critical density and the atmospheric boiling point liquid density; m_{abs} indicates the absolute adsorption capacity of hydrogen, g.

The experimental data obtained were described using Freundlich, and Langmuir adsorption models to deeper understand the relevant factors affecting H_2 adsorption capacity, which was mathematically formed as equations (4) and (5) [34,35]:

$$Q = K_{\text{F}} \cdot P^{\frac{1}{n}} \quad (4)$$

$$Q = \frac{\sum_{i=1}^N Q_{\text{e}} K_{\text{Li}} P}{1 + K_{\text{Li}} P} \quad (5)$$

Q refers to the equilibrium amount of hydrogen adsorbed per unit of adsorbent at equilibrium pressure P , K_{F} is a Freundlich adsorption equilibrium constant, n is a temperature-dependent parameter, generally $n \geq 1$. N refers to the number of different adsorption regions; Q_{ei} refers to each adsorption region's maximum hydrogen adsorption capacity; K_{Li} refers to the Langmuir adsorption equilibrium constant of the adsorption region i .

Results and discussions

To obtain the properties of biochar samples before and after activation, N_2 adsorption, thermogravimetry and hydrogen adsorption tests were performed. Some of the test results are summarized in Fig. 2.

Specific surface area and pore size distribution

To better analyze the pore structure changes of biochar materials during the activation process, we performed nitrogen

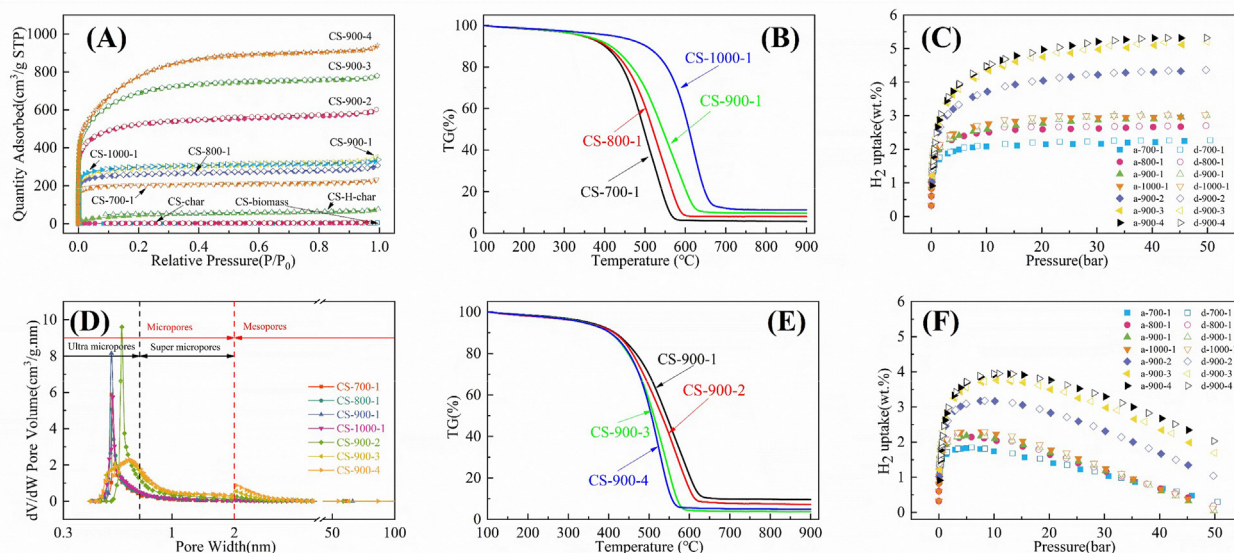


Fig. 2 – Physicochemical properties of biochar samples (A) Nitrogen adsorption isotherm (B) TG Curves at different activation temperatures (C) Absolute adsorption curve of hydrogen (D) Pore size distribution (E) TG curves of different KOH activation ratios (F) Excess adsorption curve of hydrogen.

adsorption tests on corn straw, pyrolyzed biochar at 600 °C, samples after pickling, and biochar with different activation temperatures and KOH activation ratios. Fig. 2(A) shows that the adsorption and desorption curves of biochar under different activation conditions are typical I curves. The pore structure parameters of biochar are summarized in Table 4.

Table 4 shows that the BET area of original CS-biomass is only 1.05 m²/g, and there are almost no micropores. The precipitation of volatile gases during pyrolysis at 600 °C develops the specific surface area of straw to a certain extent and promotes the growth of microporous pore structure. Compared with CS-biomass, the average pore size of pyrolysis char at 600 °C has been significantly reduced. After the pickling

treatment of H₂SO₄, the BET area of CS-char has been dramatically improved, indicating that the ash removal treatment will increase the specific surface area of biochar. This may be due to the reaction of H₂SO₄ with calcium compounds in biochar while removing some soluble inorganic salts and exchangeable metal ions (Na, K, etc.). Removing inherent minerals embedded in the coal opens up some clogged internal pore structures. Zhao et al. [36] also found that treating the coal sample with acetic acid and acetic acid enriched the coal pore structure, increasing the coal sample's specific surface area.

Using pickled biochar with a good pore structure as the initial sample can provide more reaction sites for subsequent

Table 4 – Porous structural properties of the biochar samples.

Samples	^a BET surface area (m ² /g)	^b A _{micro} (m ² /g)	^c A _{meso} (m ² /g)	^d V _{total} (cm ³ /g)	^e V _{micro} (cm ³ /g)	^e V _{meso} (cm ³ /g)	Average Pore size $f_{d_1}^g/d_2$ (nm)
CS-biomass	1.05	0	1.05	0.006	0	0.006	20.99/16.88
CS-char	10.10	7.23	2.87	0.011	0.003	0.008	4.36/8.99
CS-H-char	168.46	137.45	31.01	0.11	0.06	0.05	2.70/4.60
CS-700-1	803.85	785.74	18.11	0.36	0.31	0.05	1.79/4.10
CS-800-1	1007.61	972.85	34.77	0.47	0.40	0.07	1.86/3.83
CS-900-1	1116.69	1077.10	39.59	0.54	0.45	0.09	1.94/3.47
CS-1000-1	1155.04	1132.88	22.17	0.51	0.46	0.05	1.77/3.13
CS-900-2	1951.88	1893.25	58.64	0.93	0.82	0.11	1.91/2.70
CS-900-3	2521.93	2455.02	66.91	1.20	1.10	0.10	1.91/2.33
CS-900-4	2801.88	2705.35	96.53	1.44	1.30	0.14	2.06/2.37

^a Brunauer, Emmett and Teller (BET) method.

^b Determine by the t-plot method.

^c Obtained by the difference: Mesopore = Total pore-Micropore.

^d Determine at relative pressure P/P₀ = 0.99.

^e Determine by the H–K method.

^f Adsorption average pore diameter (4 V/A by BET).

^g BJH desorption average pore diameter (4 V/A).

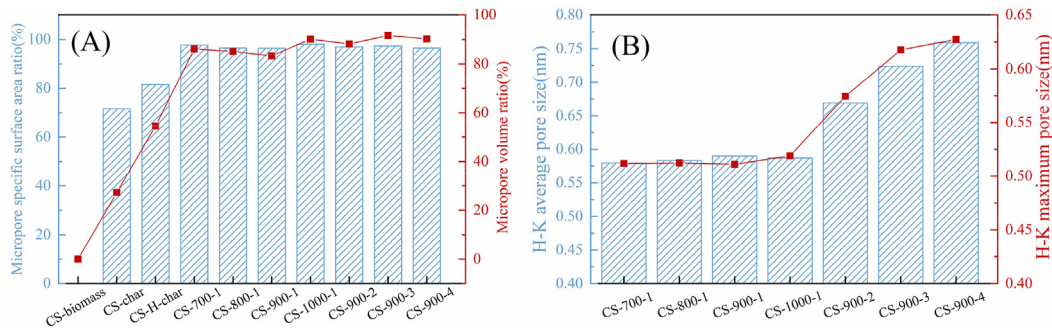


Fig. 3 – (A) Biochar sample micropores and micropore volume ratio (B) Biochar sample micropore average and maximum pore size.

activation processes. The surface area of the biochar samples obtained under different activation temperatures and KOH activation ratios was $168.46 \text{ m}^2/\text{g}$ – $2801.88 \text{ m}^2/\text{g}$, and the value span was significant, indicating that different activation carbonization treatments had a significant effect on the pore structure characteristics of biochar. In the activation temperature range of 700–1000 °C, with the increase of temperature, the growth range of BET area and microporous area of char gradually weakens. The BET area of biochar increased by 4.77, 5.98, 6.63, and 6.86 times compared with CS-H-char for each additional 100 °C from 700 °C. For biochar samples under different KOH activation ratios, the micropores have been extensively developed. The activation ratio was from 1:1 to 4:1, and the BET area of biochar expanded from 6.63 times to 16.63 times.

As the 0.5–0.7 nm is the optimal size for hydrogen storage. We focused on biochar samples' micropores and micropore volume ratio during activation. Fig. 2(D) shows that the most activated biochar pore size is concentrated in ultra-micropores. Supermicropores (0.7–2 nm) and mesopores also develop with the increased activation ratio. The average diameter and maximum diameter of micropores below 2 nm were analyzed using the H–K method, and the results are shown in Fig. 3. Fig. 3(A) shows that the proportion of biochar micropore area has significantly improved after activation. The proportion of biochar micropore area after activation under different conditions is between 96.46% and 98.08%. There is no noticeable change law between the proportion of micropore area and the activation parameters. But generally, the ratio of micropore area is maintained at a high level. Similarly, there is no evident change law for the micropore volume ratio and activation temperature and KOH activation ratio of biochar, but the average micropore volume ratio under different KOH activation ratios is more significant than that under different activation temperatures.

Fig. 3(B) shows that the average pore size and maximum pore size of biochar pores within 2 nm at different activation temperatures vary very little, with an average pore size of 0.58–0.59 nm and a maximum pore size of 0.51–0.52 nm. The results show that the activation temperature has little effect on regulating sub-nanometer pore structure. However, with the increase in the KOH activation ratio, biochar pores' average and maximum pore size increased monotonically. When the ratio of KOH/char was 4, the average pore size and maximum pore size were 0.76 nm and 0.63 nm, respectively.

Scanning electron microscope

SEM tests were carried out to study the effects of activation temperature and KOH/char ratio on the surface morphology of biochar. The specific results are shown in Fig. 4. Only four samples of CS-H-char and CS-700-1, CS-900-1, and CS-900-3 were selected for comparative analysis in this section.

From Fig. 4(A–D), the pores of straw biochar show a bundle-like structure, the surface is composed of many multi-layer pores, and the scanning electron microscope shows that the average pore size of char decreases sequentially. And the process of KOH activation is gradually expanding from the inner surface of biochar to the outer surface from the change in biochar surface morphology. When the pores of the inner surface develop to a certain extent, regular circular pores begin to appear on the outer surface.

From Fig. 4(A–a) and (A–c), the surface of the original pyrolytic char is relatively smooth, some of the surfaces have cracks, and the scanning electron microscope shows that the average pore size is about $4.17 \mu\text{m}$. However, the micropores cannot be directly observed from the SEM photos. Fig. 4(A–b) shows that the pore structure of the internal char surface has been developed to a certain extent due to the precipitation of volatile gases. Some biochar's inner surface is loose and rough, and its microporous specific surface area accounts for 81.59%. The micropore volume accounts for 54.55%, providing a pore basis and reaction site for the subsequent KOH activation process.

From Fig. 4(B), the surface cracks and pores of biochar after KOH activation increase, and the surface of the activated biochar part begins to become rough from Fig. 4(B–c). However, the outer surface as a whole is still in a relatively smooth state. The average pore size of scanning electron microscopy shows that the average pore size is about $1.82 \mu\text{m}$, which is significantly lower than that of unactivated biochar, which is consistent with the average pore change law in the nitrogen adsorption test data in Table 4. The specific surface area of micropores accounted for 97.75%, and the volume of micropores accounted for 86.11%, which indicates that KOH activation mainly increased the micropore structure.

From Fig. 4(C), with the further increase of activation temperature, the biochar surface gradually becomes rough, and the broken regular circular pore structure begins to appear. The biochar scanning electron microscope at 900 °C shows that the average pore size is about $1.74 \mu\text{m}$, slightly

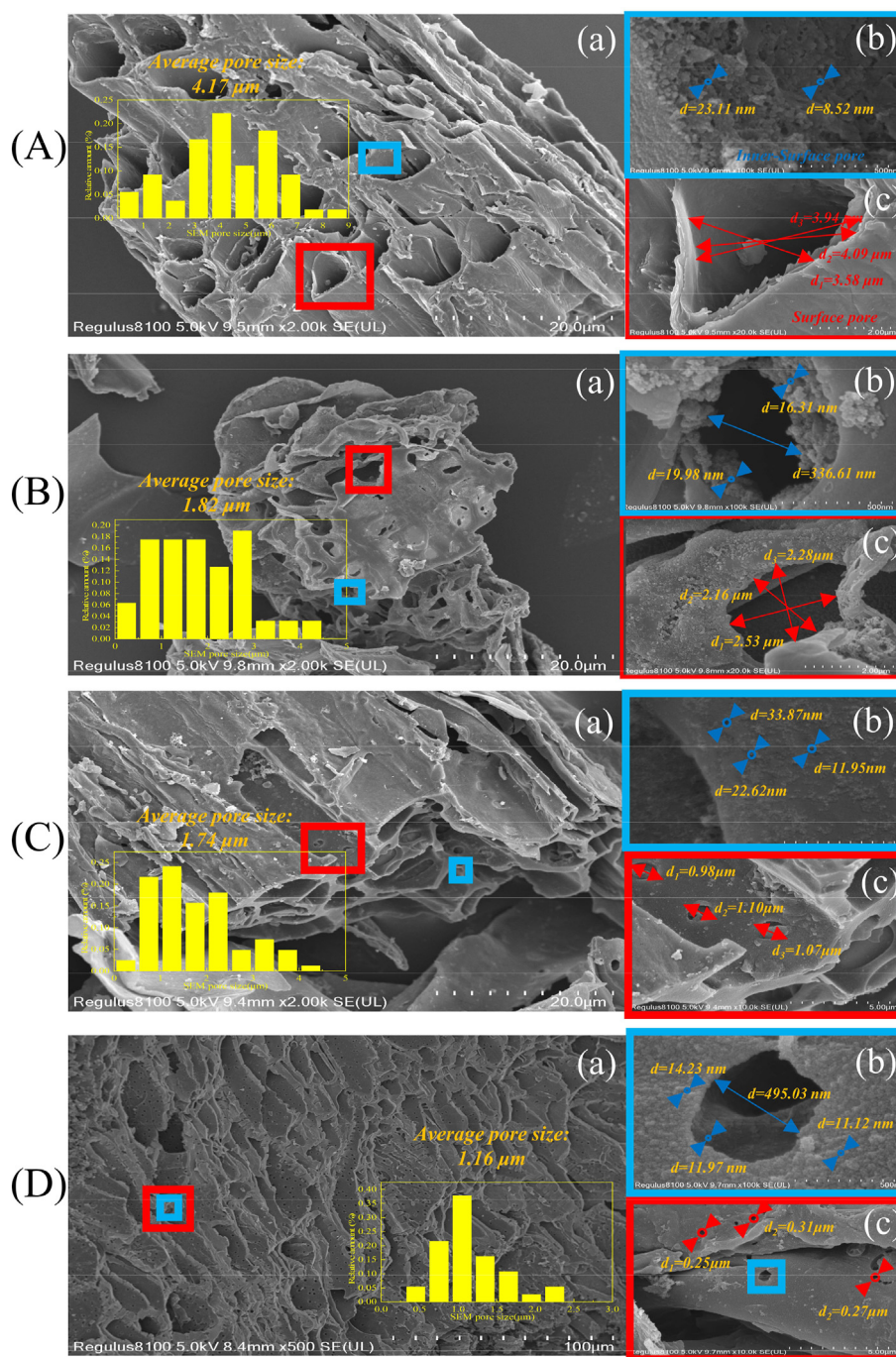


Fig. 4 – SEM analysis results of biochar samples (A) H-600-char (B) GS-700-1 (C) GS-900-1 (D) GS-900-3.

reduced compared to 700 °C. At this time, the specific surface area of micropores accounts for 96.46%, and the micropore volume accounts for 83.33%.

From Fig. 4(D), the biochar pores have been developed very thoroughly with further increase of the KOH activation ratio. Many regular circular pore structures have appeared on the outer surface. For prominent loose porous structures, KOH activation sites are distributed on biochar's inner and outer surfaces. Biochar scanning electron microscopy shows that the average pore size is about 1.16 μm , the specific surface area of micropores accounts for 97.35%, and the microporous

volume accounts for 91.67%. The regular macroporous-mesoporous-microporous structure is conducive to the adsorption of hydrogen.

Thermogravimetric analyzer test

The thermal stability of biochar samples was analyzed using an atmospheric thermogravimetric analyzer. Due to the fluctuations caused by the heating of the experimental instrument and the introduction of gas initially, we considered selecting data in the range of 100–900 °C for analysis (biochar

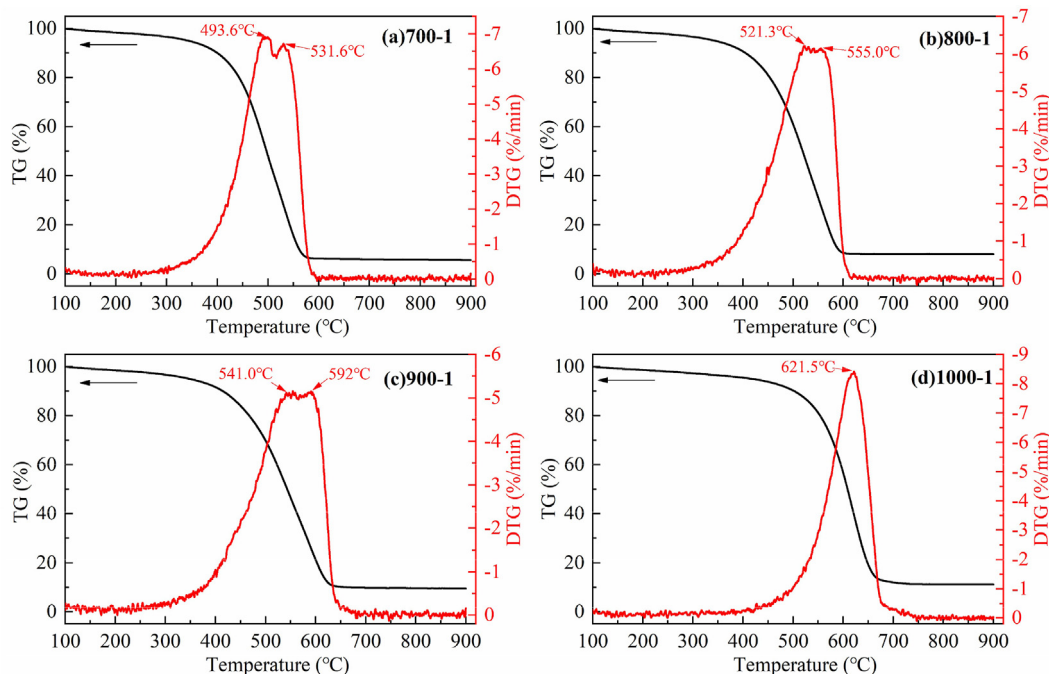


Fig. 5 – TG and DTG curves for thermogravimetric analysis testing of biochar. (a) CS-700-1 (b) CS-800-1 (c) CS-900-1 (d) CS-1000-1.

samples before 100 °C are mainly in the dehydration stage). Before each experiment, the samples dried at 105 °C for 12 h. Therefore, we believe that this treatment will have no impact on the overall data analysis. To ensure the reliability of experimental results, we carry out repeated experiments under most working conditions.

Effect of activation temperature on thermal stability of biochar
The TG and DTG curves of biochar prepared at different activation temperatures are shown in Fig. 5, it shows that the temperature range of the reaction of biochar prepared at different temperatures is 300–700 °C. Below 900 °C, the DTG curve of biochar has two prominent peaks, and when the temperature reaches 1000 °C, the peak of the reaction becomes one. With the increase of the activation temperature, the temperature range of the biochar reaction gradually narrowed and the T_p of DTG gradually increased from 493.6 °C to 621.5 °C. Since the specific surface area of biochar activated at different temperatures is between 803.85 and 1155.04 m²/g, the specific surface area is not much different. Combined with our previous research [37–39], for carbon-based materials with similar pore structures, the chemical properties of biochar mainly affect its reactivity. With the increased activation temperature, the reactive ingredients that are easy to react at this time are gradually consumed, and the reactivity is steadily weakened.

To further observe the thermal conversion characteristics of biochar, we compared the characteristic temperatures when the weight loss rate of biochar was 0.3, 0.5, and 0.7; the results are shown in Fig. 6. It shows that the characteristic temperature of biochar materials prepared at different temperatures increases with the activation temperature, regardless of the first, middle and last stages of the reaction. With the same conversion rate, compared with the biochar prepared at

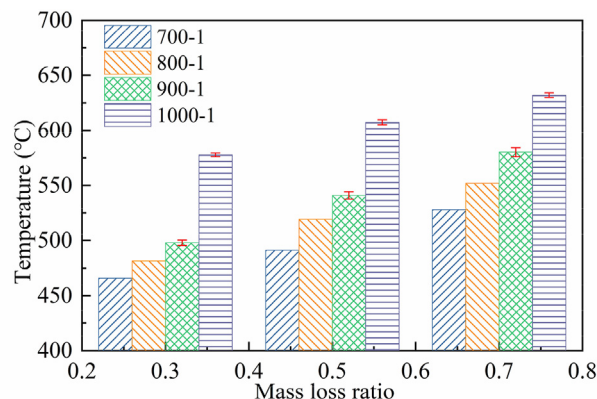


Fig. 6 – Characteristic temperature corresponding to different weight loss rates of biochar samples.

1000 °C, the characteristic temperature of the biochar samples prepared at different temperatures is quite different.

Effect of KOH activation ratio on thermal stability of biochar
The TG and DTG curves of biochar prepared with different KOH activation ratios are shown in Fig. 7, it shows that the temperature range of the reaction of biochar prepared by different KOH activation ratios is also 300–700 °C. When the ratio of KOH/char exceeds 1:1, the peak of the DTG curve reaction of biochar becomes one. Different from Fig. 6, the temperature interval of the biochar prepared by different KOH activation ratios gradually narrows, and this interval is shifted to the low-temperature region. With the KOH activation ratio increase, the T_p of DTG gradually decreased from 592 °C to 528.6 °C. Since the specific surface area of biochar activated at different temperatures is between 1116.69 and 2801.88 m²/g,

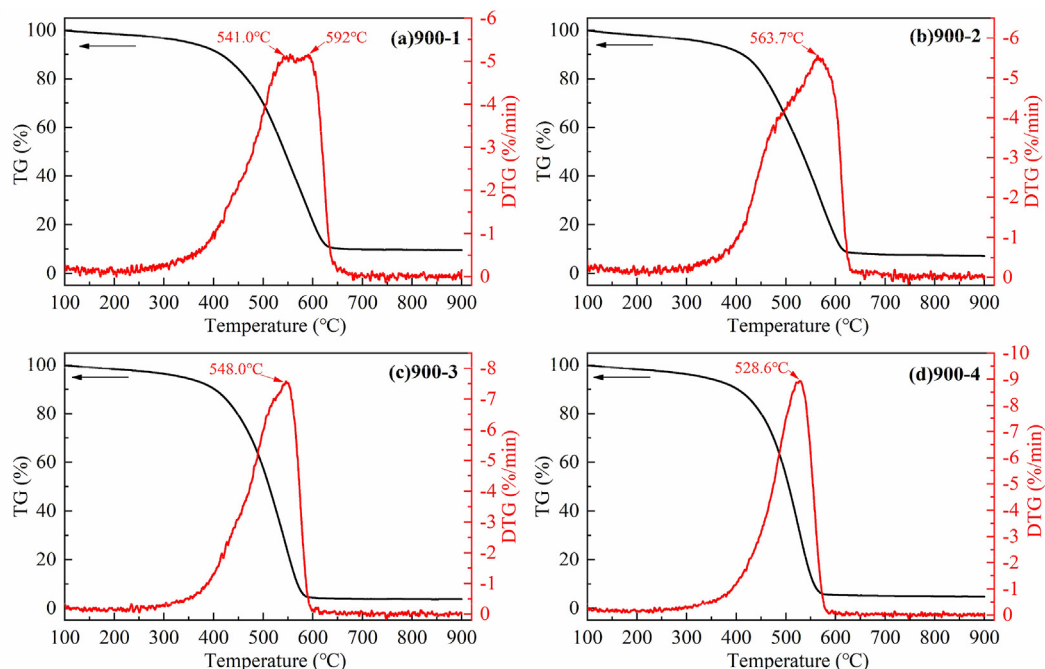


Fig. 7 – TG and DTG curves for thermogravimetric analysis testing of biochar. (a) CS-900-1 (b) CS-900-2 (c) CS-900-3 (d) CS-900-4.

the specific surface area difference between different biochar materials is considerable. So the pore structure parameters play a leading role in the reactivity of biochar in the reaction stage, and our previous research also has a similar phenomenon.

Fig. 8 shows that the characteristic temperature of biochar materials prepared with different KOH activation ratios decreases with the increase of KOH activation ratio, regardless of the first, middle and last stages of the reaction. Different from Fig. 6, the characteristic temperature difference of biochar samples prepared by different KOH activation ratios is small.

Raman spectroscopy

The Raman spectra of all biochar samples exhibited distinct G and D bands [40,41]. The Raman spectrum of biochar was

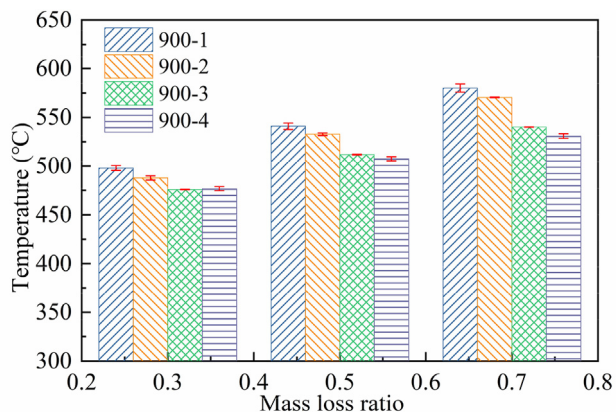


Fig. 8 – Characteristic temperature corresponding to different weight loss rates of biochar samples.

divided into five peaks, namely G, D₁, D₂, D₃, and D₄ [42,43]. Fig. 9 shows the peak fitting results of CS-700-1 Raman spectra, and Table 5 shows the fitting parameters of Raman spectra.

The I_{D1}/I_{D3} ratio, I_G/I_{All} ratio, and I_{D1}/I_G ratio are used to characterize the relative change of char chemical structure. The detailed meaning of these ratios can be found in Zhang et al. [44,45].

Fig. 10(A) shows that I_{D1}/I_{D3} , I_G/I_{All} , and I_{D1}/I_G ratios increase monotonically with the increase in activation temperature. The rise of the I_{D1}/I_{D3} ratio indicated that the increase in activation temperature promoted the transformation of biochar's small aromatic ring structure to a large aromatic ring structure. The rise in I_G/I_{All} ratio indicates that the increase in activation temperature promotes the condensation of biochar and enhances the degree of graphitization. The rise in I_{D1}/I_{D3} ratio suggested that the surface

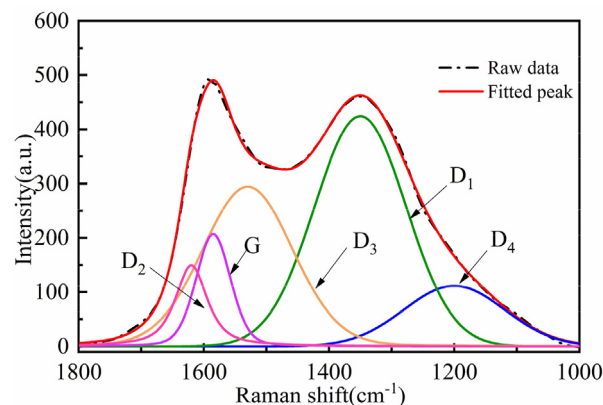


Fig. 9 – Peak fitting results of CS-700-1 Raman spectrum.

Table 5 – Fitting parameters of Raman spectrum [43–45].

Name	Peak position/cm ⁻¹	Chemical structure
D ₁	1350	C–C bond aromatic rings and aromatics with six or more rings
D ₂	1620	disordered graphitic structures.
D ₃	1530	amorphous carbon structures, aromatics with three to five rings
D ₄	1200	Caromatic-Calkyl and aromatic (aliphatic) ethers
G	1580	graphite; aromatic ring quadrant breathing; alkene C=C

Table 6 – Hydrogen storage capacity of biochar under different pressures.

Samples	H ₂ uptake (wt.%, 1 bar)	H ₂ uptake (wt.%, 10 bar)	H ₂ uptake (wt.%, 30 bar)	H ₂ uptake (wt.%, 50 bar)
CS-700-1	1.57	2.08	2.16	2.26
CS-800-1	1.84	2.50	2.62	2.70
CS-900-1	1.85	2.59	2.86	3.02
CS-1000-1	1.92	2.74	2.94	3.03
CS-900-2	2.30	3.71	4.22	4.37
CS-900-3	2.50	4.30	4.97	5.21
CS-900-4	2.53	4.44	5.20	5.32

grains of biochar were etched, the grain size decreased, and the disorder increased. This phenomenon is also consistent with the work of Pinij et al. [46], who found that the higher temperature can make the biochar form the graphite structure due to high polymerization reaction and more condensed carbon structure. Similarly, the reaction between KOH and biomass is significantly enhanced as the temperature increases, allowing the O-containing group to further transform into more stable –OH, C–O, and –COOH groups [47].

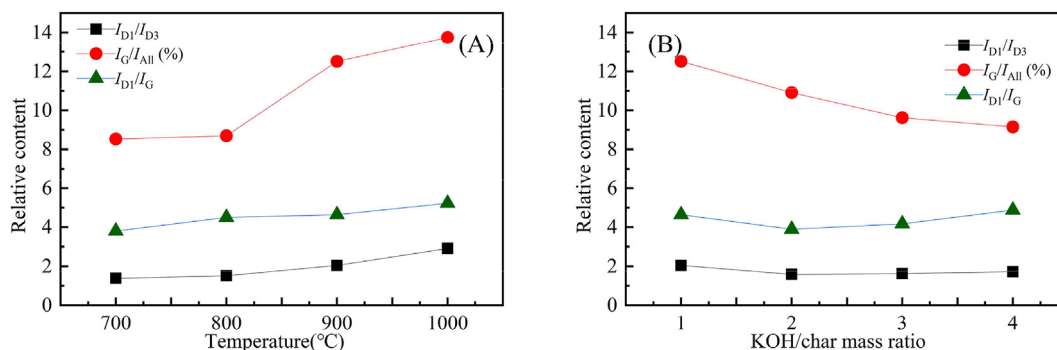
Fig. 10(B) shows that the I_G/I_{All} decreases monotonically with the activation ratio. In contrast, I_{D1}/I_{D3} and I_{D1}/I_G ratio drops first and then increases with the activation ratio. The decrease in the I_G/I_{All} indicates that the activation ratio increases the reaction between KOH, O-containing substances, and carbon fragments, creating many vacancies in biochar. OH from KOH quickly entered these vacancies to form many new O-containing groups [47], reducing the degree of graphitization of biochar. The ratio of I_{D1}/I_{D3} and I_{D1}/I_G increases first and then decreases, indicating that the KOH/char ratio is 2:1, which is the critical ratio of the chemical reaction between KOH and biochar. And Hu et al. [48] also showed that for biochar, at a lower ratio (<2:1), K can attack the oxygen site of the phenolic hydroxyl group and promote the formation of an aromatic ring with the anhydride group. However, at a higher ratio (>2:1), the surface group of the biochar gradually turns into an aromatic ring and a more stable quinone group.

H₂ storage capacity

Fig. 2(C) and (F) are the absolute adsorption-desorption and excess adsorption-desorption isotherms of hydrogen in

different biochar samples, respectively. At –196 °C, the hydrogen storage capacity of biochar was measured at 0–50 bar. And its hydrogen desorption curve almost coincided with its adsorption curve, indicating that the adsorbed and stored hydrogen was almost completely desorption and released in the pressure reduction process from high pressure to atmospheric pressure. It shows that the hydrogen release condition of biochar does not require high-temperature auxiliary conditions and only needs to reduce the pressure to achieve complete hydrogen desorption. Its reversible hydrogen storage performance is excellent, and the hydrogen desorption conditions are relatively mild.

The absolute hydrogen storage capacity of biochar under different pressures is summarized in Table 6. As the activation temperature exceeded 800 °C, the hydrogen storage capacity of biochar prepared for every additional 100 °C increased less. Compared with the biochar hydrogen storage capacity of CS-700-1, the hydrogen storage capacity of CS-1000-1 increased by 22.29%, 31.73%, 36.11%, and 34.07% at 1, 10, 30, and 50 bar, respectively. Compared with the biochar hydrogen storage capacity of CS-900-1, the hydrogen storage capacity of CS-900-4 increased by 36.76%, 71.43%, 81.82%, and 76.16% at 1, 10, 30, and 50 bar, respectively. Echoing the results of the biochar nitrogen adsorption test, the specific surface area of biochar increased significantly after 800 °C, and the increase of activation ratio fully developed the specific surface area of biochar. The relationship between hydrogen storage capacity and pore structure parameters will be further discussed below. When the pressure is 30 bar, the hydrogen storage capacity of biochar has the most significant increase ratio, while in the low-pressure area (<10 bar), the increase of specific surface

**Fig. 10 – I_{D1}/I_{D3} , I_G/I_{All} , and I_{D1}/I_G ratios vary with temperature and KOH/char ratios.**

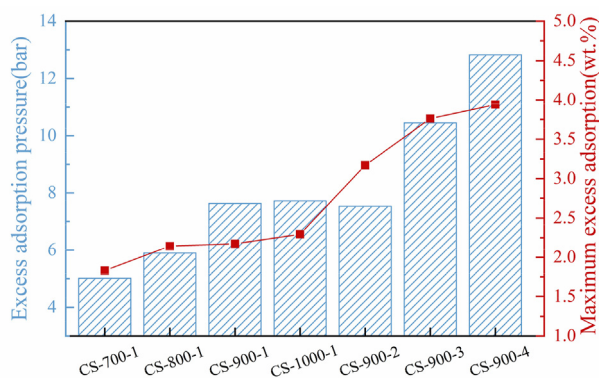


Fig. 11 – The maximum excess hydrogen adsorption capacity and corresponding adsorption pressure of different biochar.

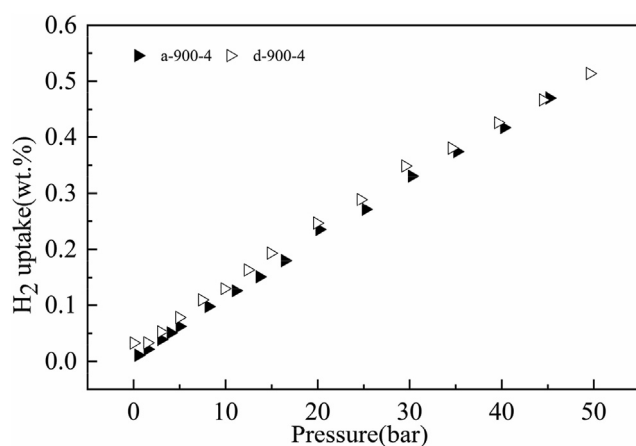


Fig. 12 – Room temperature hydrogen storage capacity of CS-900-4.

area has limited improvement in the hydrogen storage capacity of biochar.

Fig. 11 shows different biochars' maximum excess hydrogen adsorption capacity and corresponding adsorption pressure. It can be seen that the maximum excess hydrogen adsorption capacity increases from 1.83 wt% to 2.30 wt% at different activation temperatures, and the corresponding pressure increases from 5 bar to 7.72 bar, and the pressure change is small. The maximum excess hydrogen adsorption capacity increased from 2.17 wt% to 3.94 wt% under different

activation ratios, and the corresponding pressure increased from 7.64 bar to 12.83 bar.

The biochar of CS-900-4 was tested for hydrogen storage capacity at room temperature, and the test results are shown in Fig. 12. Its hydrogen storage capacity at 25 °C, 50 bar is 0.52 wt%.

Table 7 compares the hydrogen uptake of hydrogen adsorbents prepared by different carbon precursors under different thermochemical processes at -196 °C. Fig. 13 compares the hydrogen uptake at different pressures with other samples with different pore structure parameters. It shows that the hydrogen adsorbent prepared by different thermochemical processes positively correlates with its specific surface area under high-pressure or low-pressure conditions. Compared with other samples, the biochar prepared in this paper has excellent hydrogen storage capacity due to its high specific surface area and up to 96.56% microporous area.

To determine the isotherm model of hydrogen adsorption of biochar in the pressure range of 0–50 bar and to deeply understand its hydrogen adsorption mechanism, different biochar adsorption processes of hydrogen adsorption were analyzed based on the Freundlich model and Langmuir model. The three cases of $n = 1$, $n = 2$, and $n = 3$ were analyzed for the Langmuir model, and the relevant fitted model parameters are shown in Table 8. Fig. 14 shows the comparison between the Freundlich model's fitting results and the experimental results of the Freundlich model and Langmuir $n = 3$. The Langmuir model has poor consistency with the change of experimental test data when $n = 1$, the equation curve is in good agreement with experimental test data when $n = 2$ and $n = 3$, and the change law of test data is the same when $n = 3$. The Freundlich model fits slightly better than Langmuir ($n = 1$) but lower than the $n = 2$ and $n = 3$ cases. From the fitting results of different models, the adsorption of hydrogen on the pore surface of biochar is unevenly adsorbed, and the interaction force between hydrogen molecules and the pore surface is extremely inhomogeneous.

From the effects of different activation temperatures and activation ratios on the hydrogen storage capacity of biochar mentioned above, it can be found that biochar's hydrogen storage capacity at low temperatures strongly correlates with its pore structure parameters. Therefore, we further explore the relationship between the hydrogen storage capacity of different biochars and their structural characteristics (BET area, micropore area, average micropore diameter, micropore volume), the results are shown in Fig. 15. Fig. 15(A–D) shows

Table 7 – Comparison of hydrogen storage capacity of carbon at -196 °C.

References	Materials	Activation method	Hydrogen storage capacity (wt.%)	Conditions (Temperature/Pressure)
Takagi et al. (2004) [49]	Activated carbon fibers	–	2.3	1 bar
Panella et al. (2005) [13]	Activated carbon	KOH	4.5	60 bar
Wang et al. (2014) [12]	Fungus	KOH	2.4	1 bar
Rowlandson et al. (2020) [8]	Activated carbon	CO ₂	1.8	1 bar
Dogan et al. (2020) [27]	Orange peel	ZnCl	1.67	30 bar
Kızılduman et al. (2021) [3]	Rice husk	HCl	1.1	30 bar
Zhang et al. (2022) [18]	Porous carbon	Cao template method	1.53	1 bar
This work	Corn straw	KOH	2.53/5.32	1 bar/50 bar

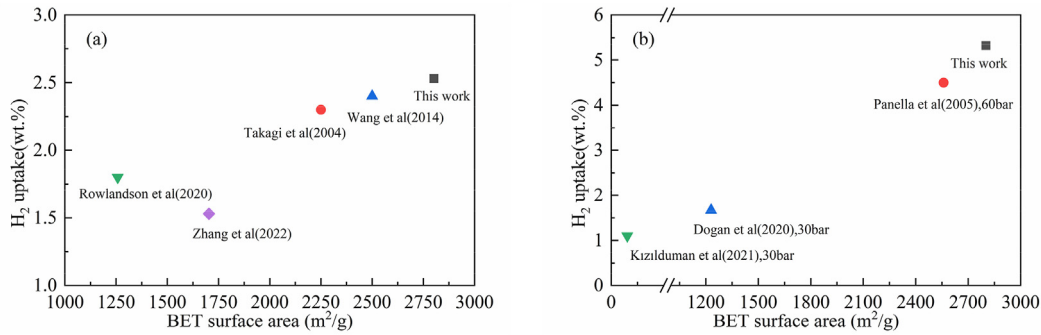


Fig. 13 – Comparison of hydrogen adsorption capacity of samples with different pore structures at $-196\text{ }^{\circ}\text{C}$ and different pressures: (a) pressure of 1 bar, (b) high pressure.

Table 8 – Freundlich (dotted line) and Langmuir isothermal adsorption model parameters of biochar.

Models	Parameters	CS- 700-1	CS- 800-1	CS- 900-1	CS- 1000-1	CS- 900-2	CS- 900-3	CS- 900-4
Freundlich	k	1.60	1.66	1.82	1.74	2.33	2.63	2.60
	n	10.44	6.96	7.32	6.25	5.70	5.33	4.91
	R ² (%)	90.09	93.80	95.57	94.45	95.10	94.67	94.70
	Reduced Chi-Sqr	0.01069	0.03857	0.01685	0.04663	0.05463	0.07627	0.10588
Langmuir n = 1	Q _e	2.15	2.54	2.77	2.83	4.15	5.01	5.21
	K _L	4.92	6.56	3.34	4.74	1.48	0.92	0.90
	R ²	90.13	93.20	87.41	94.00	92.79	94.11	95.65
	Reduced Chi-Sqr	0.01065	0.04228	0.04785	0.05042	0.08045	0.08433	0.08693
Langmuir n = 2	Q _{e1}	1.41	1.15	1.61	1.71	2.218	2.74	2.61
	Q _{e2}	0.84	1.52	1.43	1.31	2.35	2.76	3.09
	K _{L1}	19.16	76.41	22.16	0.59	7.75	0.15	4.54
	K _{L2}	0.46	0.94	0.26	40.77	0.20	4.41	0.17
	R ²	99.45	99.627	99.53	99.72	99.88	99.93	99.93
	Reduced Chi-Sqr	5.93E-04	0.00232	0.0018	0.00233	0.00129	9.53E-04	0.00148
Langmuir n = 3	Q _{e1}	0.97	0.59	1.31	1.23	1.70	1.14	2.59
	Q _{e2}	1.18	1.08	1.24	0.63	1.91	2.37	0.56
	Q _{e3}	149.78	1.05	0.82	1.20	1.05	2.09	2.61
	K _{L1}	0.94	379.52	35.36	5.90	0.10	16.47	2.05
	K _{L2}	33.89	8.96	0.91	200.06	1.66	1.24	52.39
	K _{L3}	1.62E-5	0.42	0.03	0.30	27.21	0.09	0.12
	R ²	99.79	99.97	99.93	99.98	99.99	99.99	99.97
	Reduced Chi-Sqr	2.26E-04	1.89E-04	2.69E-04	1.87E-04	8.23E-05	2.20E-04	5.92E-04

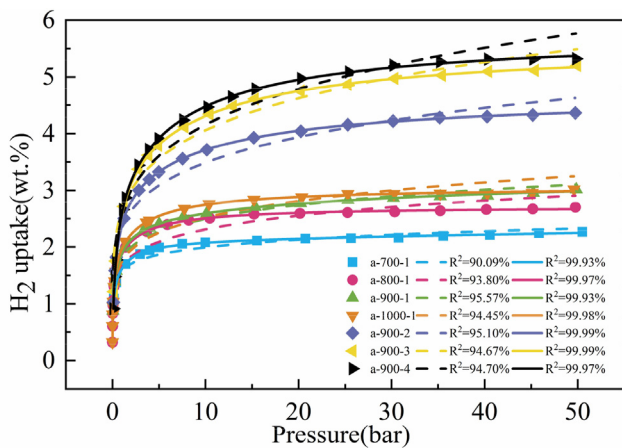


Fig. 14 – Biochar hydrogen adsorption and Freundlich (dashed line) and Langmuir N = 3 (solid line) fitting curves.

that the hydrogen storage capacity of biochar above 10 bar has an excellent linear relationship with its pore structure, among which the fitted R² with the specific surface area of the micropores is the highest, which is 98.88% at 30 bar. The low R² in the low-pressure area may be that the coverage of hydrogen adsorption is low, and due to the uneven adsorption of hydrogen by biochar, the low-pressure hydrogen storage capacity of biochar cannot be determined entirely by its physical structure. Fig. 15(A) shows that under the pressure conditions of 1, 10, 30, and 50 bar, the amount of hydrogen adsorbed by biochar per 500 BET area is 0.23 wt%, 0.59 wt%, 0.76 wt%, 0.78 wt%, which does not strictly follow Chahine's law, but the hydrogen storage capacity increases with pressure.

Therefore, from the above results, the adsorption of H₂ biochar for hydrogen under the condition of $-196\text{ }^{\circ}\text{C}$ is mainly physical adsorption. To further explore the contribution of pore structures of different sizes of biochar to

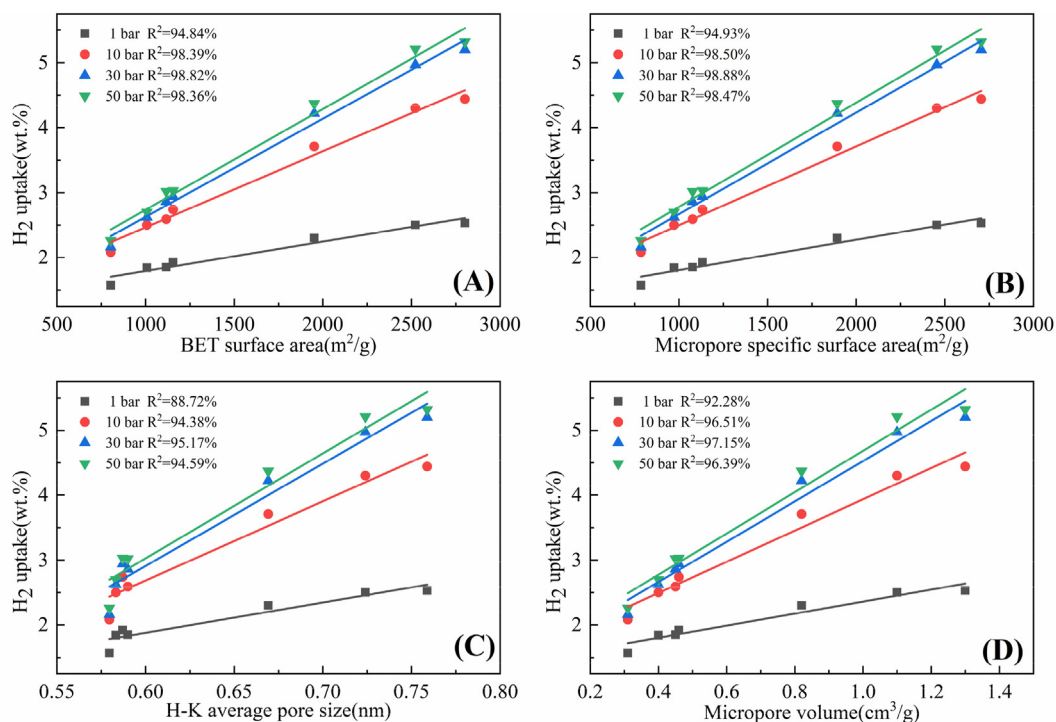


Fig. 15 – Correlation between biochar hydrogen storage capacity and its pore structure parameters (A) BET specific surface area (B) Micropore area (C) Average micropore diameter below 2 nm (D) Micropore volume.

Table 9 – The contribution of the grading pore volume to the hydrogen adsorption capacity at different pressures.

	a	b	c	d	R ²
1 bar	2.11	-0.43	2.70	-3.48	95.28
10 bar	4.01	1.11	2.04	-3.77	98.36
30 bar	5.11	1.68	2.01	0.67	98.79
50 bar	5.59	1.88	1.62	2.77	99.4

hydrogen adsorption, the following Equation (6) is defined by Canevesi et al. [50]. The polynomial linear regression method was used to explore the contribution of different grading pores to the adsorption of biochar hydrogen under different pressures. The results in Table 9 shows that ultramicropores smaller than 0.7 nm occupy a dominant position in the hydrogen storage process of biochar, and their role increases with the increase of pressure, which is consistent with the theoretical conclusions of Rzepka et al. [20], Gogotsi et al. [21], and Wang et al. [22]. The mesoporosity of biochar also has a significant influence. The low-pressure area is mainly ultramicroporous and mesoporous to determine hydrogen adsorption. Studies have shown that if carbon-based hydrogen storage materials have more mesoporous than microporous, hydrogen can be stored in mesopores, and its hydrogen storage capacity is proportional to the mesoporous volume [3,51]. The high-pressure region is transformed into ultra-micropores, while other pores also provide a place for hydrogen adsorption, and the role of macropores at 50 bar begins to be highlighted.

$$y = aV_{<0.7} + bV_{0.7-2} + cV_{2-50} + dV_{>50} \quad (6)$$

Conclusions and prospects

The process of KOH melt activation was adjusted to control the nanopore structure of biochar to prepare an adsorbent with high hydrogen adsorption capacity. A series of characterizations of the prepared biochar were carried out, and its hydrogen absorption characteristics were discussed. The prepared biochar has a very high microporous ratio above 96.46%. The specific surface area of biochar prepared under suitable activation conditions was 2801.88 m²/g, and the absolute adsorption capacity of hydrogen was 2.53 wt% at 1 bar and reached 5.32 wt% at 50 bar. The KOH activation process gradually turns from the inside of biochar to the outside, forming regular circular holes on the surface. The thermal stability of biochar increases with the activation temperature and decreases with the activation ratio. The fitting curve of the Langmuir model ($n = 3$) almost coincides with the experimental test curve, and the adsorption of hydrogen on the pore surface of biochar is inhomogeneous. The hydrogen storage capacity of biochar above 10 bar has a good linear relationship with its pore structure, and the fitting R² with the specific surface area of the micropores is the highest. Ultramicropores smaller than 0.7 nm occupy a major position in the hydrogen storage process of biochar, and the role of macropores under 50 bar also begins to be highlighted. In the low-pressure area, ultramicropores and mesopores determine hydrogen adsorption.

This paper removes AAEMs in biochar that may affect its hydrogen storage capacity. The relationship between the physical structure of biochar and its hydrogen storage capacity was studied. The linear correlation between the

adsorption capacity and the pore structure parameters in the low-pressure area was not high, which may be affected by the surface chemical structure. Future research will be further carried out in this regard to achieve the goal of high-density hydrogen storage of biochar under milder conditions.

Declaration of competing interest

The authors declare that they have no known competing financial interests or personal relationships that could have appeared to influence the work reported in this paper.

Acknowledgements

This work is supported by the Fundamental Research Funds for the Central Universities (2022ZFJH004).

REFERENCES

- [1] Xiao Y, Dong H, Long C, Zheng M, Lei B, Zhang H, et al. Melaleuca bark based porous carbons for hydrogen storage. *Int J Hydrogen Energy* 2014;39:11661–7.
- [2] Fierro V, Zhao W, Izquierdo MT, Aylon E, Celzard A. Adsorption and compression contributions to hydrogen storage in activated anthracites. *Int J Hydrogen Energy* 2010;35:9038–45.
- [3] Kızılduman BK, Turhan Y, Doğan M. Mesoporous carbon spheres produced by hydrothermal carbonization from rice husk: optimization, characterization and hydrogen storage. *Adv Powder Technol* 2021;32:4222–34.
- [4] Xia Y, Yang Z, Zhu Y. Porous carbon-based materials for hydrogen storage: advancement and challenges. *J Mater Chem* 2013;1:9365–81.
- [5] Blankenship LS, Mokaya R. Cigarette butt-derived carbons have ultra-high surface area and unprecedented hydrogen storage capacity. *Energy Environ Sci* 2017;10:2552–62.
- [6] Blankenship LS, Balahmar N, Mokaya R. Oxygen-rich microporous carbons with exceptional hydrogen storage capacity. *Nat Commun* 2017;8:1545.
- [7] Gayathiri M, Pulingam T, Lee KT, Sudesh K. Activated carbon from biomass waste precursors: factors affecting production and adsorption mechanism. *Chemosphere* 2022;294:133764.
- [8] Rowlandson JL, Edler KJ, Tian M, Ting VP. Toward process-resilient lignin-derived activated carbons for hydrogen storage applications. *ACS Sustainable Chem Eng* 2020;8:2186–95.
- [9] Ramesh T, Rajalakshmi N, Dhathathreyan KS. Activated carbons derived from tamarind seeds for hydrogen storage. *J Energy Storage* 2015;4:89–95.
- [10] Chen T, Zhou Y, Luo L, Wu X, Li Z, Fan M, et al. Preparation and characterization of heteroatom self-doped activated biocarbons as hydrogen storage and supercapacitor electrode materials. *Electrochim Acta* 2019;325:134941.
- [11] Zhang Y, Wang S, Feng D, Gao J, Dong L, Zhao Y, et al. Functional biochar synergistic solid/liquid-phase CO₂ capture: a review. *Energy & Fuels* 2022;36:2945–70.
- [12] Wang J, Senkovska I, Kaskel S, Liu Q. Chemically activated fungi-based porous carbons for hydrogen storage. *Carbon* 2014;75:372–80.
- [13] Panella B, Hirscher M, Roth S. Hydrogen adsorption in different carbon nanostructures. *Carbon* 2005;43:2209–14.
- [14] Sun Y, Webley PA. Preparation of activated carbons from corncob with large specific surface area by a variety of chemical activators and their application in gas storage. *Chem Eng J* 2010;162:883–92.
- [15] Isinkaralar K, Gullu G, Turkyilmaz A, Dogan M, Turhan O. Activated carbon production from horse chestnut shells for hydrogen storage. *Int J Glob Warming* 2022;26:361–73.
- [16] Poirier E, Chahine R, Bose TK. Hydrogen adsorption in carbon nanostructures. *Int J Hydrogen Energy* 2001;26:831–5.
- [17] Bénard P, Chahine R. Determination of the adsorption isotherms of hydrogen on activated carbons above the critical temperature of the adsorbate over wide temperature and pressure ranges. *Langmuir* 2001;17:1950–5.
- [18] Zhang H, Zhu Y, Liu Q, Li X. Preparation of porous carbon materials from biomass pyrolysis vapors for hydrogen storage. *Appl Energy* 2022;306:118131.
- [19] Cabria I, López MJ, Alonso JA. The optimum average nanopore size for hydrogen storage in carbon nanoporous materials. *Carbon* 2007;45:2649–58.
- [20] Rzepka M, Lamp P, de la Casa-Lillo MA. Physisorption of hydrogen on microporous carbon and carbon nanotubes. *J Phys Chem B* 1998;102:10894–8.
- [21] Gogotsi Y, Portet C, Osswald S, Simmons JM, Yildirim T, Laudisio G, et al. Importance of pore size in high-pressure hydrogen storage by porous carbons. *Int J Hydrogen Energy* 2009;34:6314–9.
- [22] Wang Q, Johnson JK. Molecular simulation of hydrogen adsorption in single-walled carbon nanotubes and idealized carbon slit pores. *J Chem Phys* 1998;110:577–86.
- [23] Zhao W, Fierro V, Zlotea C, Aylon E, Izquierdo MT, Latroche M, et al. Optimization of activated carbons for hydrogen storage. *Int J Hydrogen Energy* 2011;36:11746–51.
- [24] Romanos J, Beckner M, Rash T, Firlej L, Kuchta B, Yu P, et al. Nanospace engineering of KOH activated carbon. *Nanotechnology* 2011;23: 015401.
- [25] Wang S, Lee Y-R, Won Y, Kim H, Jeong S-E, Wook Hwang B, et al. Development of high-performance adsorbent using KOH-impregnated rice husk-based activated carbon for indoor CO₂ adsorption. *Chem Eng J* 2022:135378.
- [26] Huang C-C, Chen H-M, Chen C-H. Hydrogen adsorption on modified activated carbon. *Int J Hydrogen Energy* 2010;35:2777–80.
- [27] Doğan M, Sabaz P, Bıcıl Z, Koçer Kizilduman B, Turhan Y. Activated carbon synthesis from tangerine peel and its use in hydrogen storage. *Journal of the Energy Institute* 2020;93:2176–85.
- [28] Feng D, Zhao Y, Zhang Y, Xu H, Zhang L, Sun S. Catalytic mechanism of ion-exchanging alkali and alkaline earth metallic species on biochar reactivity during CO₂/H₂O gasification. *Fuel* 2018;212:523–32.
- [29] Sun H, Feng D, Sun S, Zhao Y, Zhang L, Chang G, et al. Effect of acid washing and K/Ca loading on corn straw with the characteristics of gas-solid products during its pyrolysis. *Biomass Bioenergy* 2022;165:106569.
- [30] Williams NE, Oba OA, Aydinlik NP. Modification, production, and methods of KOH-activated carbon. *ChemBioEng Reviews* 2022;9:164–89.
- [31] Zornitta RL, Barcelos KM, Nogueira FGE, Ruotolo LAM. Understanding the mechanism of carbonization and KOH activation of polyaniline leading to enhanced electrosorption performance. *Carbon* 2020;156:346–58.
- [32] Feng D, Zhang Y, Zhao Y, Sun S, Wu J, Tan H. Mechanism of in-situ dynamic catalysis and selective deactivation of H₂O-activated biochar for biomass tar reforming. *Fuel* 2020;279:118450.
- [33] Feng D, Guo D, Zhang Y, Sun S, Zhao Y, Shang Q, et al. Functionalized construction of biochar with hierarchical

- pore structures and surface O/N-containing groups for phenol adsorption. *Chem Eng J* 2021;410.
- [34] Salvador F, Montero J, Sánchez-Montero MJ, Izquierdo C. Mechanism of heterogeneous adsorption in the storage of hydrogen in carbon fibers activated with supercritical water and steam. *Int J Hydrogen Energy* 2011;36:7567–79.
- [35] Jung M-J, Kim JW, Im JS, Park S-J, Lee Y-S. Nitrogen and hydrogen adsorption of activated carbon fibers modified by fluorination. *J Ind Eng Chem* 2009;15:410–4.
- [36] Zhao H, Wang B, Li Y, Song Q, Zhao Y, Zhang R, et al. Effect of chemical fractionation treatment on structure and characteristics of pyrolysis products of Xinjiang long flame coal. *Fuel* 2018;234:1193–204.
- [37] Zhang WD, Zhao YJ, Sun SZ, Feng DD, Li PF. Effects of pressure on the characteristics of bituminous coal pyrolysis char formed in a pressurized drop tube furnace. *Energy & Fuels* 2019;33:12219–26.
- [38] Deng L, Zhang W, Sun S, Bai C, Zhao Y, Feng D, et al. Study on the thermal conversion characteristics of demineralized coal char under pressurized O₂/H₂O atmosphere. *Fuel* 2021:122429.
- [39] Deng L, Zhang W, Sun S, Bai C, Zhao Y, Feng D, et al. Effect of pressure on the structure and reactivity of demineralized coal during O₂/H₂O thermal conversion process. *Energy* 2021:122632.
- [40] Oginni O, Singh K, Oporto G, Dawson-Andoh B, McDonald L, Sabolsky E. Influence of one-step and two-step KOH activation on activated carbon characteristics. *Bioresour Technol* 2019;234:100266.
- [41] Yumak T, Bragg D, Sabolsky EM. Effect of synthesis methods on the surface and electrochemical characteristics of metal oxide/activated carbon composites for supercapacitor applications. *Appl Surf Sci* 2019;469:983–93.
- [42] Sheng C. Char structure characterised by Raman spectroscopy and its correlations with combustion reactivity. *Fuel* 2007;86:2316–24.
- [43] Sonibare OO, Haeger T, Foley SF. Structural characterization of Nigerian coals by X-ray diffraction, Raman and FTIR spectroscopy. *Energy* 2010;35:5347–53.
- [44] Zhang W, Sun S, Zhao Y, Zhao Z, Wang P, Feng D, et al. Effects of total pressure and CO₂ partial pressure on the physicochemical properties and reactivity of pressurized coal char produced at rapid heating rate. *Energy* 2020:208.
- [45] Zhang W, Zhao Y, Sun S, Feng D, Li P. Effects of pressure on the characteristics of bituminous coal pyrolysis char formed in a pressurized drop tube furnace. *Energy & Fuels* 2019;33:12219–26.
- [46] Pinij P, Tippayawong N, Chimupala Y, Chaiklangmuang S. Performances of functional groups and KOH-transformation in corn stover waste through catalytic pyrolysis. *J Anal Appl Pyrol* 2021;157:105234.
- [47] Chen W, Gong M, Li K, Xia M, Chen Z, Xiao H, et al. Insight into KOH activation mechanism during biomass pyrolysis: chemical reactions between O-containing groups and KOH. *Appl Energy* 2020;278:115730.
- [48] Hu M, Ye Z, Zhang Q, Xue Q, Li Z, Wang J, et al. Towards understanding the chemical reactions between KOH and oxygen-containing groups during KOH-catalyzed pyrolysis of biomass. *Energy* 2022;245:123286.
- [49] Takagi H, Hatori H, Soneda Y, Yoshizawa N, Yamada Y. Adsorptive hydrogen storage in carbon and porous materials. *Mater Sci Eng, B* 2004;108:143–7.
- [50] Canevesi RLS, Schaefer S, Izquierdo MT, Celzard A, Fierro V. Roles of surface chemistry and texture of nanoporous activated carbons in CO₂ capture. *ACS Appl Nano Mater* 2022;5:3843–54.
- [51] Xia K, Gao Q, Wu C, Song S, Ruan M. Activation, characterization and hydrogen storage properties of the mesoporous carbon CMK-3. *Carbon* 2007;45:1989–96.